In-situ Construction of Ceria-Metal/Titanate Heterostructure with Controllable Architectures for Efficient Fuel Electrochemical Conversion

Shuai He,[†] Meng Li,[‡] Jianing Hui,[†] and Xiangling Yue[*, †]*

[†]School of Chemistry, University of St Andrews, St Andrews, Fife, KY16 9ST, UK

[‡]Energy and Environmental Science and Technology, Idaho National Laboratory, Idaho Falls, ID 83415, USA

*Corresponding author: xy57@st-andrews.ac.uk

KEYWORDS: Titanate perovskite, CeO_2 exsolution, co-exsolution, tunable heterostructure, SOFCs

ABSTRACT: Construction of ceria-metal/titanate heterostructure via exsolution is a promising strategy to improve the catalytic activity of titanate perovskites and broaden their applications in various energy conversion scenarios. However, the species exsolved after reduction are limited to reducible metal cations, such as Ni, Co, Fe, and precious metals. Herein, we report a modified exsolution approach for co-exsolving active oxides and metal nanoparticles from a titanate perovskite, $La_{0.8}Ce_{0.1}Ni_{0.4}Ti_{0.6}O_{3-\delta}$ (LCeNT). We highlight strained facet-specific CeO_2 cubes can be grown on the support after an air-annealing process with their morphology tunable by varying

annealing temperature, whilst exsolution of Ni nanoparticles form subsequently following chemical/electrical reduction. An electrolyte-supported SOFC utilizing CeO_2-Ni@LCeNT anode achieves maximum power density of 642 mW cm^{-2} at 900 ℃ in H_2 (~3% H_2O). Exceptional robustness of the heterostructure is illustrated after running the cell in CH_4 (~3% H_2O) for 20 hrs. Overall, this work demonstrates an intriguing pathway to constructing stable and active ceria-metal/titanate heterostructure for energy applications.

1. Introduction

Titanate perovskites consisting of various alkaline and/or rare earth metals at the A-site have been continuing to attract a great deal of attention in various fields, including catalysis and energy applications [1-3]. This is due to their capability of accommodating multiple oxidation states at the B-site, which catalyzes various oxidation/reduction reactions and provides superior conductivity [4-7]. Besides, titanates are relatively stable against carbon deposition and redox cycling, offering excellent efficiency and durability for long-term operation [8-11]. Nevertheless, the broad utilization of titanate is hindered by its insufficient electrocatalytic activity when compared with that of the conventional nickel-based catalysts [12, 13].

Modification of titanate to enhance its catalytic properties is therefore imperative to enable its wider application. Creating heterostructure is one of the predominant methods for fabricating highly active materials in catalytic and electrocatalytic systems. By carefully designing the heterointerface, the attributes of a heterostructure could be efficiently tuned. Impregnation is a widely used and economically feasible technique for dispersing nanoparticles (NPs) on titanate surface to build heterostructures. Titanates decorated with impregnated CeO_2-Ni nanostructures were reported to demonstrate substantially improved electrochemical performance for fuel

oxidation, making it a good candidate for electrochemical systems [14-16]. Lu *et al.* infiltrated CeO_2 and Ni NPs into a $La_{0.2}Sr_{0.25}Ca_{0.45}TiO_3$ (LSCT) backbone in an anode-supported solid oxide fuel cell (SOFC), which exhibited a remarkably boosted electrochemical oxidation activity, achieving a peak power density of 0.96 W cm^{-2} at 800 °C in H_2 [16]. Disturbingly, the infiltrated NPs are found prone to aggregating at elevated temperatures due to their weak particle-substrate interactions, leading to inevitable performance degradation with extended operation time. A heterostructure with thermodynamically stable catalyst NPs can be alternatively built by *in-situ* exsolution, which has attracted intensive interests in recent years due to the inherently stronger particle-substrate interaction and diverse catalyst components it introduced. So far, the studies have been focused on the exsolution of singular transitional metal or alloy catalysts from titanates [17-21].

In this work, we aim to develop an approach to co-exsolve ceria and Ni nanoparticles and construct the ceria-Ni/titanate heterostructure *in situ* from a titanate substrate, $La_{0.8}Ce_{0.1}Ni_{0.4}Ti_{0.6}O_{3-\delta}$ (LCeNT). A previous report attempted to co-exsolve CeO_2-Ni NPs from the same titanate backbone by a single reduction treatment (1000 °C in 5% H_2/Ar) [17], however, despite a diffraction peak of ceria and that of metallic Ni detected by X-ray diffraction, CeO_2 nanostructure was never microscopically evidenced on the surface of the titanate and as such, application of this material with both ceria and Ni NPs from exsolution has not been reported to the best of the authors' knowledge. In contrast, the approach developed in the present work consists of an air-annealing process and a subsequent reduction treatment, from which nanoscale ceria cubes featuring $\{111\}_{CeO2}$ facets and Ni NPs were successfully constructed respectively on the surface of the parent titanate perovskite. The heterostructure, specifically the heterointerface between CeO_2 and LCeNT support, was tuned by varying annealing temperature, yielding different

size and population in ceria nanocubes. The underlying mechanism for the controllable ceria exsolution was explored. The application of this new heterostructure was exemplified as a SOFC anode, with its performance and stability evaluated in H_2 and/or CH_4 fuels. The contribution of the exsolved ceria nanostructure and the ceria-Ni/titanate heterostructure was assessed and discussed towards the electro-oxidation of H_2 and CH_4.

2. Experimental

2.1. Material synthesis and sample preparation

$La_{0.8}Ce_{0.1}Ni_{0.4}Ti_{0.6}O_{3-\delta}$ perovskite, as a substrate for co-exsolving ceria and Ni nanostructure, was fabricated via a modified solid-state synthesis method, following the procedures in Ref [11]. A stoichiometric amount of dried La_2O_3 (Pi-Kem, 99.99%), CeO_2 (Acros, 99.9%), $Ni(NO_3)_2 \cdot 6H_2O$ (Acros, 99%) and TiO_2 (Alfa Aesar, 99.6%) were mixed homogeneously, and after that, the mixture was calcined at 1000 ℃ for 12 hrs. The resultant precursor was ball-milled for 2 hrs, followed by a final firing at 1400 ℃ for 12 hrs to form a pure perovskite phase. Following the same procedure, $La_{0.43}Ca_{0.37}Ni_{0.1}Ti_{0.9}O_{3-\delta}$ was prepared using La_2O_3, $CaCO_3$ (Alfa Aesar, 99.99%), $Ni(NO_3)_2 \cdot 6H_2O$ and TiO_2. LCNT served as a comparing composition with only metallic Ni exsolution after reduction, removing the effect of ceria contribution as encountered in LCeNT.

The as-synthesized LCeNT and LCNT were ground in an agate mortar and then ball-milled with a planetary ball miller for 2 hrs to obtain fine powders with an average particle size of ~3 μm and ~2 μm, respectively. The LCeNT fine powder was mixed with 10 wt.% rice starch (Sigma-Aldrich, US) as pore former and pressed into pellets, followed by calcination at 1400 ℃ for 2 hrs. To introduce exsolved ceria phase, the prepared pellets were annealed at different temperatures ranging from 800 ℃ to 1400 ℃ for 2 hrs in ambient air to study the effect of temperature on the

segregation of ceria particles. The annealed samples were named with annealing temperature following LCeNT, *e.g.* LCeNT800, LCeNT1100, *etc*. thereafter. The generation of metallic Ni NPs happened during a reduction of the annealed samples at 900 ℃ in 5% H_2/Ar flow. A sample without annealing treatment was also reduced under the same conditions, referred to as rLCeNT herein.

2.2. Material Characterizations

2.2.1 X-ray diffraction (XRD)

Room temperature XRD was used to analyze the phase purity and crystal structure of the as-synthesized powder and those treated at varying temperatures and after reduction. Pellet-form samples were crushed into powders using agate mortar and pestle for XRD analysis. XRD measurement was performed on a PANalytical Empyrean X-ray diffractometer with Cu-$K_{\alpha 1}$ radiation in reflection mode, and the samples were scanned from 10 to 90 degrees with a step size of 1.3 º/ min. The obtained XRD patterns were then analyzed with Xpert HighScore plus software to confirm the crystal structure. Rietveld refinement was done on selected data using GSAS-II software to determine the unit cell parameters and the weight fraction of any secondary phase [22]. A set of refined parameters include linear background interpolation, scale factor, unit cell parameters, peak profile parameters *u*, *v,* and *w*, sample displacement, atomic positions, site occupancies, and thermal factor for individual atom sites, similar to that reported previously [23].

2.2.2. Scanning electron microscopy (SEM)

The porous LCeNT pellets' surface morphology before and after annealing/reduction was characterized by a FEI Scios Dual-Beam Focused Ion Beam – Scanning Electron Microscope (FIB-SEM, FEI company, US). Backscattered electron (BSE) mode was adopted as well in some

cases to highlight the compositional variation. The working voltage for imaging was 5 kV. Energy-dispersive X-ray analysis (EDS) was conducted at 15 kV to identify elemental compositions of a specific area. The studied pellet samples include as-prepared LCeNT (reference) and annealed LCeNT before and after reduction.

2.2.3. Scanning transmission electron microscopy (STEM)

High resolution high-angle annular dark-field STEM (HAADF-STEM) imaging, EDS, and EELS analysis were performed at 200 kV using a scanning transmission electron microscope equipped with an objective Cs aberration corrector (FEI Titan Themis 200, fitted with a Super-X windowless EDX detector). TEM and EDS allow us to inspect the microstructural and compositional information of the material before and after various treatments, and EELS enables us to identify the valence state of Ce in the as-prepared and annealed LCeNT.

Thin LCeNT lamellae, as TEM/EDS/EELS sample, were prepared from the pellet samples using the Scios microscope in FIB mode, at a voltage of 30 kV with Ga^+ ion source. A typical FIB milled lamella containing desirable surface nanostructures is displayed in **Figure S1**. The final lamella was around 50 nm in thickness, ideal for further atomic resolution examination.

2.3. *Electrochemical characterization*

2.3.1. Fuel cell fabrication

All cells fabricated in the present study had identical electrolyte and air electrode configurations, with a sole variation in fuel electrode. $Zr_{0.89}Sc_{0.1}Ce_{0.01}O_{2-\gamma}$ (ScSZ) electrolyte (thickness in the range of 120 - 130 µm) was made by tape casting and sintering at 1400 °C. Electrodes having an active area of 0.5 cm^2 were introduced by screen-printing on both sides of the dense ScSZ electrolyte, which served as support to the electrodes. LCeNT ink was prepared by mixing the

perovskite powder (average particle size ~3 μm) with dispersant and organic binder. $(La_{0.8}Sr_{0.2})_{0.95}MnO_3$ (LSM)-ScSZ (50:50 by weight), pure LSM, and LCNT inks were prepared in a similar fashion. After screen printing, the LCeNT fuel electrode was fired at 1200 ℃ while the LSM based air electrode was fired at 1100 ℃. The thickness of both electrodes was in the range of 20-30 μm. Gold paste/wires were used for current collection on both fuel electrode and air electrode. An overview of the single cell can be found in **Figure S2**, which shows the sandwiched cell configuration of LCeNT|ScSZ|LSM-ScSZ|LSM (namely LCeNT cell). The cell with LCNT fuel electrode (*i.e.* LCNT|ScSZ|LSM-ScSZ|LSM) was prepared and evaluated using similar procedures to help understand the catalytic contribution from exsolved ceria in the LCeNT electrode.

2.3.2. Electrochemical testing

The ScSZ-supported button cell was amounted to the testing jig and sealed to the fuel chamber with ceramic paste (Ceramabond 552, Aremco). The assembly was then placed in a vertical temperature-controlled furnace. To firstly demonstrate the contribution of CeO_2 exsolution on anode performance, the LCeNT and LCNT cells (noted as Cell-1 and Cell-2, respectively) were heated to 900 ℃ in N_2 (40 mL min^{-1}) with their performance assessed in wet H_2 and CH_4 (3% H_2O, 40 mL min^{-1}) fuels subsequently. It was believed that Ni exsolution was at a minimum in this manner in both electrodes; therefore its contribution towards cell performance could be excluded and as a result, the main difference in performance between Cell-1 and Cell-2 can be attributed to the exsolved ceria participation in catalytic reactions on SOFC anode.

To construct the ceria-metal/titanate (namely CeO_2-Ni@LCeNT) electrode, 5% H_2/N_2 (40 mL min^{-1}) gas was introduced to a fresh LCeNT cell (Cell-3) and maintained for 20 hrs at 900 ℃ to exsolve Ni NPs. In addition to the chemical reduction (CR), the fuel electrode was further reduced

electrically by applying an electrolysis potential to it (electrical reduction, namely ER). In contrast to the lengthy CR process (~20 hrs), it is reported that applying a high electrolysis voltage can almost instantly reduce the titanate perovskite, generating numerous nanocatalysts (*e.g.* Ni NPs) on its surface and thus reinforcing catalytic activity [24, 25]. Therefore, a voltage of 2.1 V was employed to Cell-3 after CR at 900 ℃ to boost cell performance further. This was done in wet H_2 (3% H_2O) for 20 min in total, with 5 min in each cycle. During the course of the electrochemical test, the fuel electrode was fed with a wet (3% H_2O) H_2 or CH_4 stream at a constant flow rate of 40 mL min^{-1}, while the air electrode was exposed to ambient air.

Impedance, current density-voltage (I-V) and stability characteristics of the cells were measured using a Solartron 1470B instrument coupled with a 1252A frequency response analyzer. Impedance data with AC voltage amplitude of 10 mV and frequency ranging from 100 kHz to 100 mHz were collected under open-circuit voltage (OCV) conditions. A stability test of the CeO_2-Ni@LCeNT cell (Cell-3) was conducted in wet CH_4 under a constant voltage of 0.7 V at 850 ℃.

3. Results and discussion

3.1. Characteristics of pristine LCeNT

Figure 1a displays the Rietveld refined XRD characteristic reflections of the as-prepared LCeNT and rLCeNT at room temperature. A pure orthorhombic perovskite structure is seen for the pristine LCeNT, confirming the successful synthesis of the A-site deficient titanate in air. The pure phase titanate is further evidenced by its smooth and clean surface microstructure in **Figure 1b**, with compositions closely matching the expected stoichiometric ratio as measured using STEM-EDS (**Figure S3**). After reducing the as-prepared LCeNT in 5% H_2/Ar at 900 ℃ for 20 hrs, a small yet noticeable peak can be seen at 44.5° in the XRD pattern in Figure 1a. It indicates

the exsolution of Ni metal, which is accompanied by a slight lattice expansion (~0.42%) in perovskite. As a support to this, densely packed NPs can be seen on the surface of rLCeNT (in **Figure 1c**).

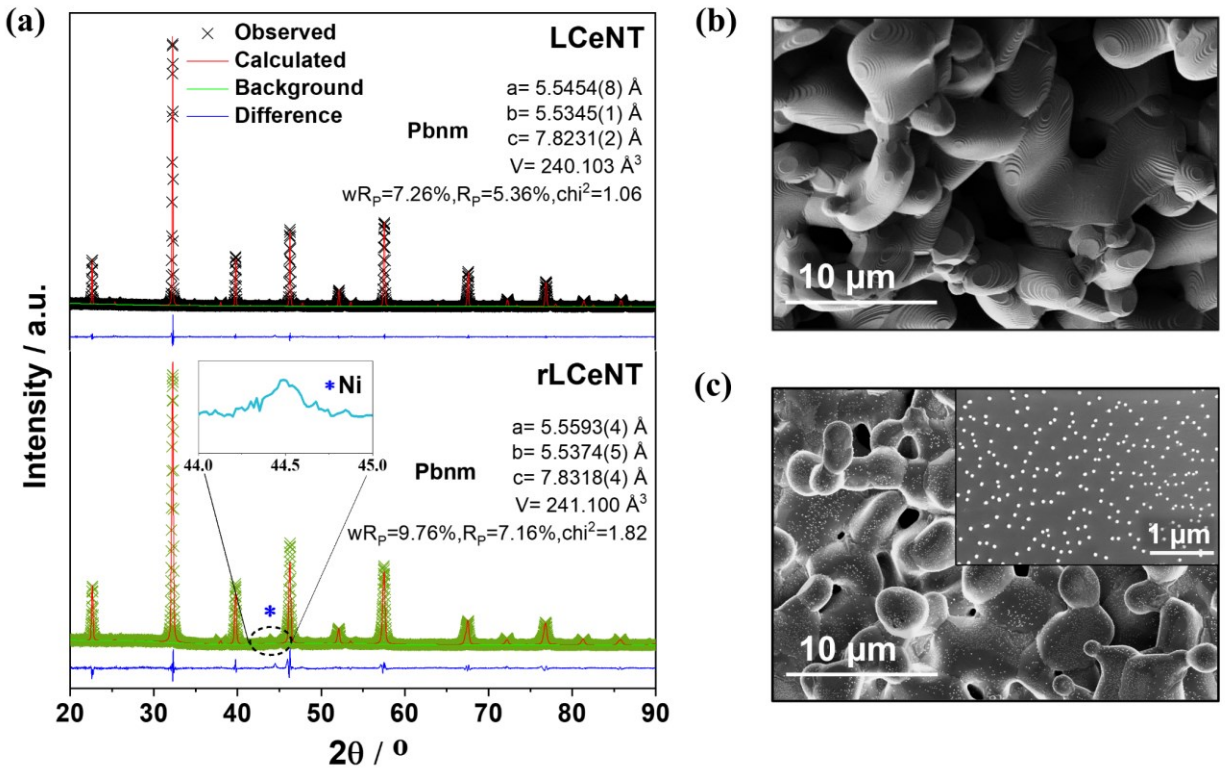

Figure 1. (a) Rietveld refined XRD patterns of the as-prepared LCeNT and rLCeNT; SEM micrographs of (b) the as-prepared LCeNT and (c) reduced LCeNT (rLCeNT) after flowing 5% H_2/Ar at 900 ℃ for 20 hrs

The absence of CeO_2 in both XRD and SEM-EDS (Figure 1c and **S4**) analysis of rLCeNT suggests no evident CeO_2 precipitation occurred after reduction under 5% H_2/Ar at 900 ℃ for 20 hrs. According to an earlier study, the co-exsolution of a fluorite-type structure (possibly CeO_2) and Ni was induced after reducing LCeNT at 1000 ℃ in a diluted hydrogen atmosphere [17]. It was assumed such fluorite phase reflected the possible presence of reduced $CeO_{2-\delta}$, which was

triggered by the high local depletion of Ni on the B-site and the significant distortion in the perovskite caused by the undersized $Ce^{3+/4+}$. Nevertheless, no direct proof of microscopic observations of CeO_2 was reported, and the material was adopted for catalytic applications merely based on exsolved Ni nanoparticles functioning as a catalyst. This altogether implies the exsolution of readily observable CeO_2 phases is not guaranteed in reducing atmosphere, especially at lower temperatures that are close to operating temperature in catalytic and/or electrocatalytic applications (*e.g.* 900 °C in our work). Alternatively, we disclose, for the first time, facet specific CeO_2 cubes can be grown *in situ* by annealing the pristine LCeNT in air, with the exsolved nanostructure tunable by varying temperature, and the titanate perovskite with decorated ceria cubes is still capable of exsolving numerous metallic Ni NPs when exposed to reducing atmosphere, thus yielding a hierarchical structure with ceria and Ni NPs on titanate surface. This will be discussed in detail in the following sections.

3.2. A-site exsolution of CeO_2 cubes

3.2.1. Annealing induced CeO_2 growth

Upon air-annealing the pristine LCeNT at 1200 °C, numerous cube-like nanostructures (~220 nm in size) grow on the surface of titanate in **Figure 2a**, which is a distinct feature comparing to the smooth surface topography of the as-prepared counterpart (Figure 1b). As evidenced by the XRD analysis (in **Figure S5b**), the cube-like structure is most likely CeO_2 due to the appearance of its $\{111\}_{CeO2}$ main reflection peak at 28.6° [26], indicating the segregation of ceria from the perovskite lattice during annealing. It appears that the LCeNT perovskite structure only experiences a slight unit cell volume shrinkage (~0.11%), rather than decomposition, as a result of the segregation of CeO_2 nanocubes.

The faceted ceria cubes develop a well-socketed interface structure on the substrate without any visible cracks or voids, explicitly revealed by the cross-sectional STEM imaging in **Figure 2b**. The STEM-EDS analysis was performed at the CeO_2/LCeNT interface area to study the elemental distribution across the exsolved interface, and the results are illustrated in **Figure 2(b, c)**. The EDS line scan spectrum and element maps prove that the cube consists of cerium and oxygen, with a ratio of 1: 2 matching the stoichiometric value of ceria. It means that the Ce component in the exsolved cubes predominantly exists as Ce (IV).

High-resolution STEM imaging was conducted to investigate the crystalline structure of the exsolved CeO_2 cube, as shown in **Figure 2(d, e)**. The atomic geometry of the faceted ceria cube is characterized by the densely packed and periodically arranged Ce atoms, and the fast Fourier transform (FFT) pattern of the ceria single crystal implies its octahedral cubic structure. In addition, the edge lattice fringes of the ceria cube with the spacing of 0.348 nm and 0.305 nm can be indexed to $\{111\}_{CeO2}$ and $\{200\}_{CeO2}$ planes, respectively. Unlike randomly orientated ceria NPs, the well-ordered ceria cubes consisting of multiple termination facets and orientations were suggested to possess two times higher activity per surface area for CO_2 conversion [27]. Comparing to a typical cubic cerium oxide, where $d_{\{111\}}$= 0.311 nm, $d_{\{200\}}$= 0.269 nm [28], in our experiment the lattice of the exsolved ceria cube seems to be notably expanded, indicating a strained crystal structure, which will be discussed further in the following part.

Figure 2 (f, g) presents the high-resolution STEM images of the interface between an exsolved CeO_2 cube and the LCeNT substrate. The measured lattice fringe spacings of 0.348 nm and 0.305 nm of the substrate can be indexed to the $\{111\}_{LCeNT}$ and the $\{200\}_{LCeNT}$ planes, respectively. These are identical to the exsolved ceria single crystal, as shown in Figure 2 (d, e), indicating the epitaxial growth of CeO_2 cubes with an expanded lattice structure. The exsolution of the ceria

epitaxy, which is thermodynamically favorable, minimizes the interfacial strain due to lattice mismatch between the two phases. As shown in Figure 2g, the atom geometry at a cube/substrate interfacial region exhibits an abrupt transition from one phase to the other with no observable micropores in between, suggesting a coherent interface structure. The closely packed Ce atoms well align to the B-site cations of the titanate, which reflects a parallel orientation relationship between the two lattices. A similar coherent heterointerface structure was observed by Neagu *et al.* at the epitaxially grown Ni/$La_{0.4}Sr_{0.4}Ni_{0.03}Ti_{0.97}O_{3-\gamma}$ substrate interface, stressing that such well-pinned interface architecture was beneficial not only for providing superior stability of the exsolved NPs against aggregation but also for facilitating the ion interdiffusion process between the two phases [29].

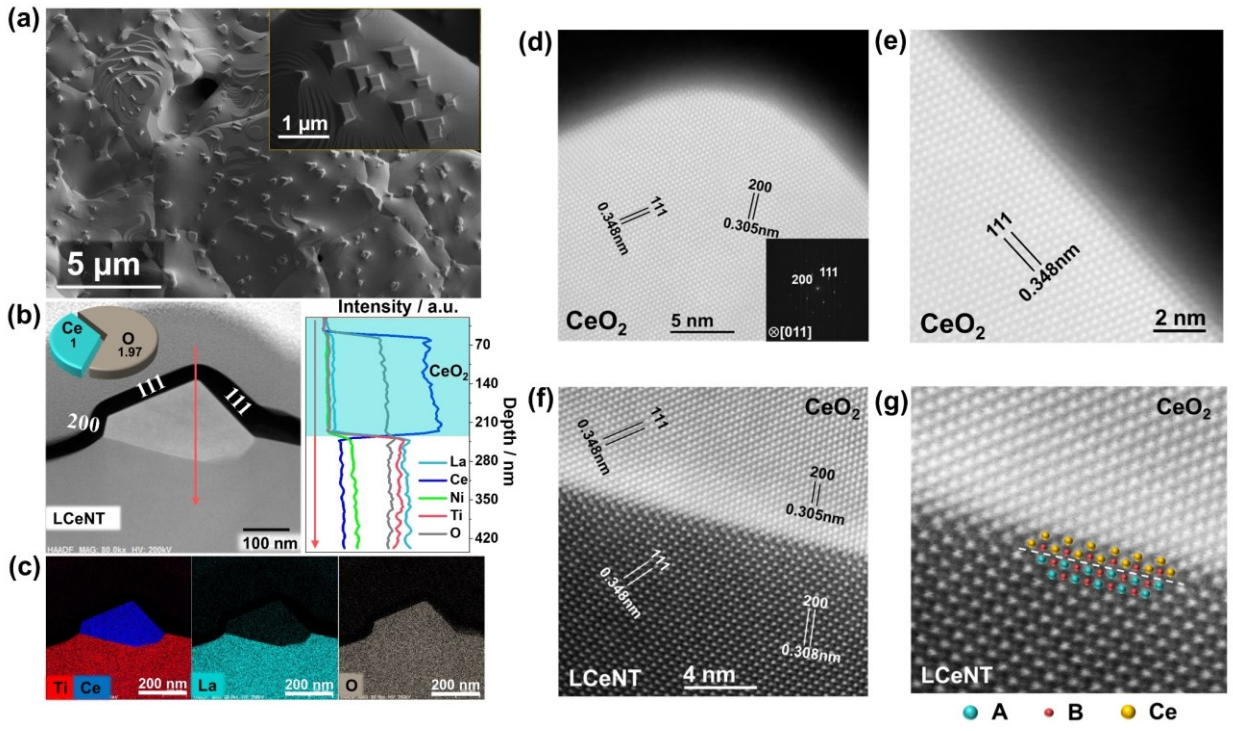

Figure 2. Microstructure and element distribution of LCeNT1200. (a) SEM micrographs of the titanate surfaces after annealing at 1200 ℃; (b) STEM-HAADF image of an exsolved ceria nanocube and the corresponding EDS line scan spectrum. The upper grey and black bands are

carbon protection layers deposited during FIB milling. The inserted arrows and pie chart indicate the direction of the corresponding EDS line scan, and the rough atomic ratio between Ce and O, respectively; (c) STEM-EDS element mapping showing the element distribution across the exsolved titanate interface; (d, e) High-resolution STEM images of the terminating facets of an exsolved CeO_2 cube, taken along CeO_2[011] zone axis; (f, g) atomic geometry at the CeO_2/LCeNT interface.

3.2.2. Temperature-controlled ceria growth

The exsolution of ceria cubes from LCeNT is found sensitive to annealing temperatures; hence the microstructures of the as-synthesized LCeNT annealed at different temperatures in the range of 1300-800 ℃ for a fixed 2 hrs duration were monitored. It is aimed that by adjusting the annealing conditions, ceria cubes with desirable size and surface coverage can be grown.

Figure 3 shows the BSE micrographs of the surface morphology of LCeNT annealed at 1300, 1200, 1100, 1000, 900, and 800 ℃ respectively, and **Figure 4 (a, b)** displays the corresponding XRD patterns after annealing at these temperatures. The behavior of ceria cube exsolution as a function of annealing temperature is illustrated by a schematic diagram shown on the right-hand side in Figure 3. Depending on the annealing conditions, the size of exsolved ceria cubes and their population vary greatly. At 1300 ℃, there are no obvious CeO_2 cubes emerging on the surface of the titanate grain. Nevertheless, some stripe-shaped ceria phase can be seen along the grain boundaries, which is confirmed by the appearance of a small peak at 28.5°, corresponding to CeO_2, on the XRD pattern in Figure 4 a-b. **Figure 4c** illustrates the weight fraction of exsolved ceria and the corresponding unit cell shrinkage of the parent LCeNT as a function of annealing temperature, which is acquired based on the Rietveld refinement analysis of XRD patterns (**Figure S5**). Worth noting that the weight fraction of the ceria dopant in pristine LCeNT is approximately 7.6 wt.%.

Compared to the pristine LCeNT, around one-third of ceria segregated from the titanate (~2.7 wt.%) after annealing at 1300 ℃, accompanied by a ~0.16% cell volume shrinkage in perovskite. When annealing temperature drops to 1200 ℃, the exsolution of ceria can also be seen from the XRD pattern in Figure 4 (a, b). However, the morphology of ceria now displays pronounced faceting on the surface of the substrate in Figure 3. Comparing to 1300 ℃, lowering annealing temperature leads to a gradual decrease in the normalized intensity of the ceria diffraction peak in Figure 4b, indicating lowered ceria segregation extent with temperature, *e.g.*, ~1.4 wt.% of ceria weight fraction and 0.11% of perovskite volume shrinkage after annealing at 1200 ℃.

As the annealing temperature drops to 1100 ℃, substantial exsolution of fine CeO_2 cubes takes place on the titanate surface, as shown in the BSE image in Figure 3, revealing ceria cubes with a much smaller size (~130 nm *vs* ~220 nm) and larger population (~9 particles per μm^2 *vs* ~1 particle per μm^2) as compared to those after annealed at 1200 ℃. It should be noted that although the exsolution of ceria cubes at 1100 ℃ is seen under SEM, the diffraction peak of CeO_2 cannot be detected by XRD. This is most likely due to the low amount of ceria exsolved at reduced temperatures, which is below the detection limit of the diffractometer employed (<1 wt.%). Further decrease in annealing temperature gives rise to the formation of even smaller ceria cubes (*e.g.* ~55 and ~40 nm in cube size, and ~20 and ~10 particles per μm^2 in cube density at 1000 and 900 ℃, respectively). The precipitation of CeO_2 cubes from the substrate seems to disappear after annealing at 800 ℃, which is possibly originated from the insufficient thermal energy for the bulk diffusion of Ce cations at such a low temperature.

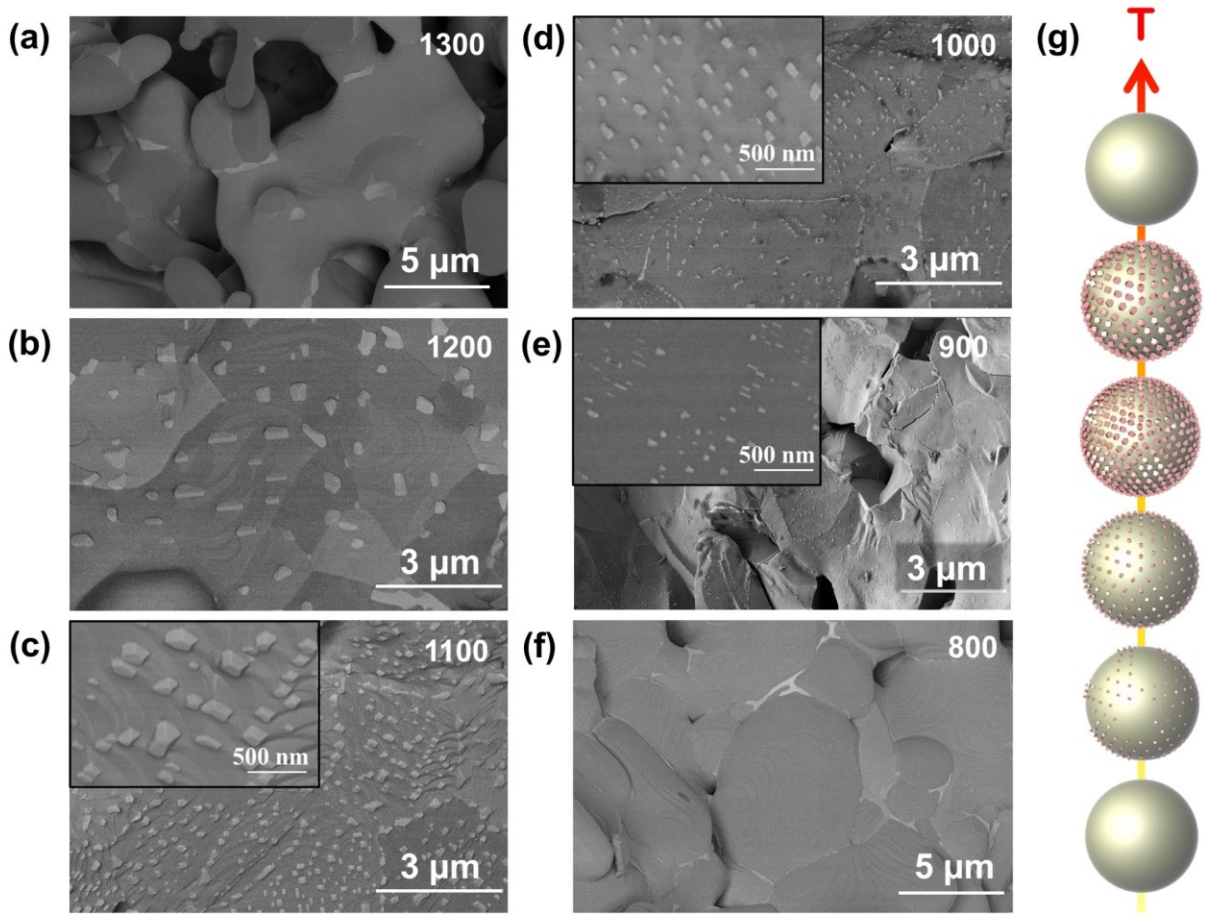

Figure 3. Backscattered electron micrographs of LCeNT pellet surfaces annealed at (a) 1300, (b) 1200, (c) 1100, (d) 1000, (e) 900, and (f) 800 ℃ for 2 hrs in air, respectively, and a (g) schematic diagram showing the trend of CeO_2 cube exsolution as the temperature increases (from bottom to top).

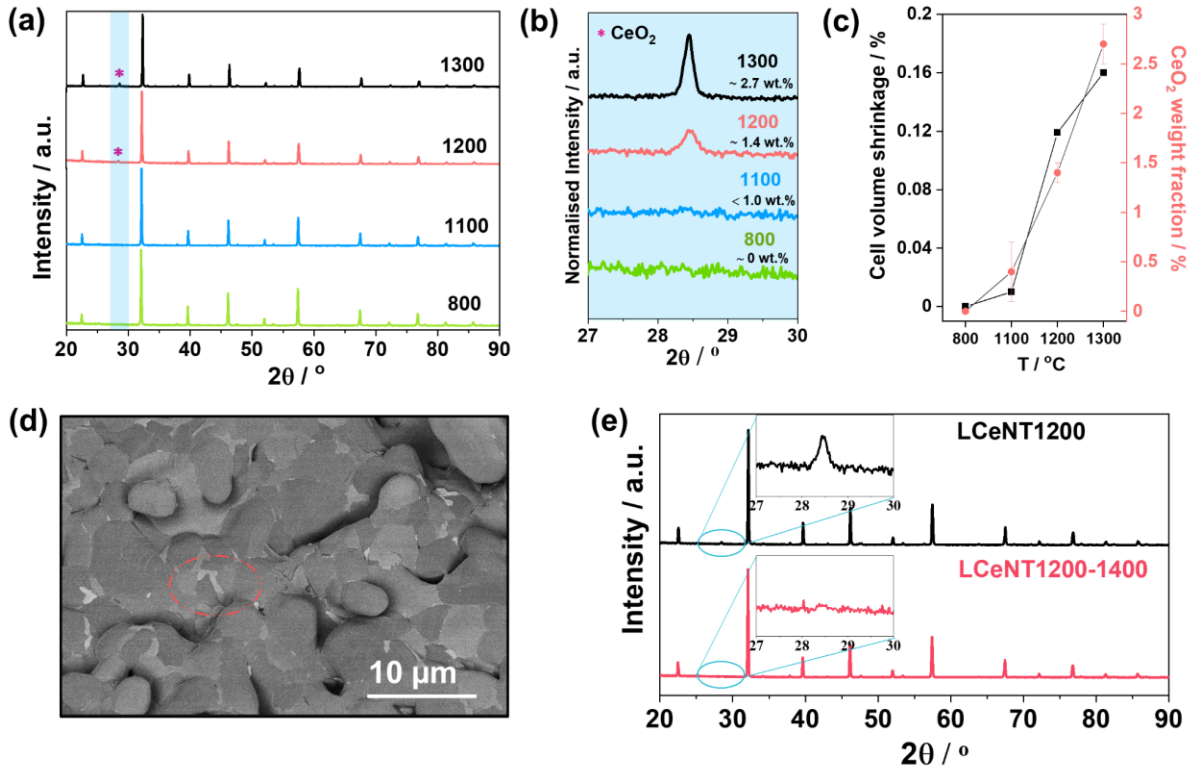

Figure 4. (a) XRD reflections of LCeNT annealed at 1300, 1200, 1100 and 800 ℃ for 2 hrs and (b) the magnified area showing CeO_2 (111) peak with rough quantification results obtained from Rietveld refinement, (c) LCeNT unit cell shrinkage following ceria exsolution as well as exsolved CeO_2 weight fraction as a function of annealing temperature, (d) BSE image of the LCeNT1200 surface after treated at 1400 ℃ for 2 hrs in air and (e) the corresponding XRD patterns. The dashed circle in (d) highlights the presence of a possible ceria phase.

To examine whether the exsolved CeO_2 phase can be re-incorporated back into the underlying perovskite lattice, we fired the LCeNT1200 at 1400 ℃ in the air for 2 hrs, namely LCeNT1200-1400. **Figure 4d** shows the BSE image of the surface morphology of LCeNT1200-1400. After being subjected to high temperature again, the exsolved ceria cubes on the grain surfaces disappear,

with some small patches of possible ceria phase (highlight by a dashed circle in Figure 4d) left at the grain boundaries of the substrate. Compared to LCeNT1200, the absence of the ceria reflection peak in the XRD pattern in **Figure 4e** confirms that most of the exsolved ceria have been re-incorporated into the underlying perovskite structure after being subjected to 1400 ℃. A low magnification SEM micrograph of the LCeNT1200-1400 is provided in **Figure S6** where it is compared to that of LCeNT1300, with the latter having significant ceria segregation along grain boundaries (confirmed by XRD in Figure 4b).

Herein, we propose a feasible method for adjusting the ceria exsolution by taking advantage of the annealing temperature, which could grow CeO_2 cubes with desired size and population on the substrate surface. Since the exsolved ceria phase is re-dissolvable, it could be advantageous to regenerate the particle-substrate interfaces after degradation despite the high operation temperature required; however, this needs further investigation.

3.2.3. Mechanistic understanding of CeO_2 exsolution

Based on the results discussed so far, it appears that the incorporation of ceria in the titanate was successful at 1400 ℃ in air during the initial synthesis, producing a pure orthorhombic perovskite structure. When annealed at lower temperatures (1300 ℃~ 900 ℃), up to one-third of the doped ceria in LCeNT segregated from the perovskite lattice, forming patch-like structure on grain boundaries at 1300 ℃ and cubes with different sizes on the surface of the substrate at lower than 1300 ℃. Upon firing at 1400 ℃ again, the segregated ceria can re-dissolve into the underlying titanate lattice. It seems temperature is a critical factor affecting the dissolution/segregation of ceria in titanate perovskite. Worth noting that although ceria exsolution will introduce higher A-site deficiency (α) to the LCeNT structure (where $\alpha = 0.1$), earlier studies suggested that similar titanate perovskites are capable of accommodating an A-site deficicency of up to 0.2 without

decomposition [17, 30]. It is therefore unsurprising to see the persisted perovskite structure after ceria exsolution (up to one third of doped level, see Figure 4a) in our study. Herein, we propose that the incorporation of ceria into LCeNT perovskite at 1400 ºC and the ceria segregation/dissolution from the perovskite structure at 1300-900 ºC involve (a) thermal reduction at high temperature during synthesis, (b) low-temperature oxidation, and (c) titanate lattice strain relaxation during annealing.

The incorporated Ce in the as-prepared LCeNT was often considered Ce (IV), as the titanate was fabricated in air using CeO_2 as a starting material [17]. However, Ce (IV) cations have been found too small to fit into the A-site of the titanate perovskite, which causes significant lattice strain and distortion [31-33]. Some researchers found in their study that ceria can only be successfully doped in titanate under a reducing atmosphere, with cerium preferentially occupying the A-site as Ce (III) [33-35]. Indeed, the presence of Ce (III) in the pristine LCeNT in the present work is unambiguously revealed by the EELS analysis (**Figure 5a**), though cerium doping into the A site of titanate was realized through the solid-state synthesis in air. The characteristics and intensity ratio of Ce M_4, M_5 edges in EELS have been used to determine the oxidation states of Ce [36-38]. Buseck *et al.* reported that for Ce^{4+}, $M_{4,5}$ peaks feature two shoulder peaks (named as B and B′) at higher energies, while the peak intensity ratio $I(M_5)/[I(M_4)+I(M_5)]$ is around 0.49; for Ce^{3+} only one shoulder peak (named as A) is observed at lower energy of M_4, and the peak intensity ratio is around 0.55 [37]. In Figure 5a, the peak intensity ratio $I(M_5)/[I(M_4)+I(M_5)]$ is close to 0.55, and the Ce M_4 edge is more asymmetrical than the M_5 edge, though less obvious due to the low concentration of Ce, with a shoulder peak A at 896.4 eV. These features suggest the dominant presence of Ce (III) in pristine LCeNT. As a comparison, **Figure 5b** shows the EELS spectrum of Ce acquired from an exsolved CeO_2 cube. The $M_{4,5}$ peaks of Ce in ceria cube can be identified by

two shoulder peaks, B and B', originated from transitions to 4f states in the conduction band [39]; the intensity of M_5 peak is lower than that of M_4, distinct from what is observed in Figure 5a. These characteristics denote the Ce (IV) nature of cerium in the exsolved nanostructure, in line with the EDS analysis in Figure 2b.

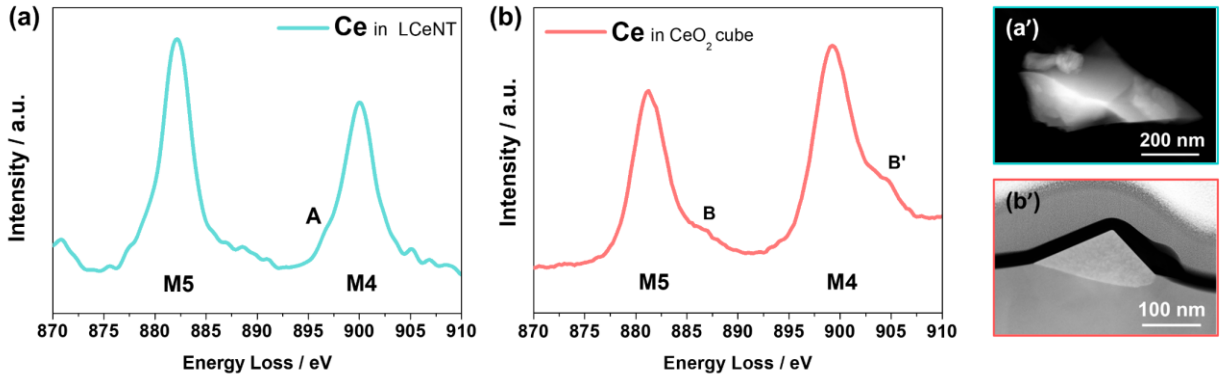

Figure 5. A comparison of Ce EELS spectra acquired from (a, a') an as-prepared LCeNT particle and (b, b') an exsolved ceria cube.

Cumming *et al.* [31, 40] also reported the presence of Ce^{3+} at the A-site of the doped $SrTiO_3$ after sintering in air at 1400 °C. It seems that Ce^{4+} is reduced to Ce^{3+} during synthesis to occupy the A-site of the titanate perovskite. Such a phenomenon, commonly referred to as thermal reduction, has been widely observed in many oxide systems [41-46], which generally requires a high temperature (≥ 1400 °C) and a low oxygen partial pressure (< 10^{-7} bar) [41]. Gokon *et al.* [45] evaluated the activity of CeO_2 at thermal reduction temperatures of 1300-1500 °C for the two-step water-splitting reaction. The CeO_2 material treated at a higher temperature was found to result in a higher reduction extent and thus, a higher hydrogen production rate. Following several prerequisites, the thermal reduction process has been well explained by a charge compensation model proposed by Peng *et al.* [47]. In the case of La (III) substitution by Ce (IV) in the present

work, the defect models describing the processes that occurred during the synthesis of LCeNT can be written in Kröger-Vink notation:

$$4La_{La}^{\times} + 3Ce^{4+} \rightleftarrows 3Ce_{La}^{\cdot} + V_{La}^{'''} + 4La^{3+} \quad (1)$$

$$V_{La}^{'''} \rightleftarrows V_{La}^{\times} + 3e \quad (2)$$

$$3Ce_{La}^{\cdot} + 3e \rightleftarrows 3Ce_{La}^{\times} \quad (3)$$

Overall:

$$4La_{La}^{\times} + 3Ce^{4+} \rightleftarrows 3Ce_{La}^{\times} + V_{La}^{\times} + 4La^{3+} \quad (4)$$

The above defect models depict that Ce (IV) cations are thermally reduced to Ce (III) during high temperature synthesis, and then incorporated into the A-site of the titanate perovskite.

During the annealing in the temperature range of 1300 ℃ to 900 ℃, the conditions required for thermal reduction no longer exist, on the contrary, oxidation of Ce^{3+} dopant in LCeNT occurs, generating many undersized Ce^{4+} cations on the A-site of the titanate (*i.e.* $r_{Ce4+,\ CN=12}$= 1.14 Å *vs* $r_{La3+,\ CN=12}$=1.36 Å). Such significant cation size discrepancy consequently drives the Ce^{4+} dopant out of the host lattice, with numerous patch and cube-like ceria precipitates on the titanate grain boundaries and surfaces, respectively, depending on annealing temperature. When the annealing temperature decreases to below 900 ℃, the ambient environment cannot provide enough thermal energy for the above processes to proceed, in addition to the sluggish relaxation of the strain in the perovskite lattice which retards the cation diffusion. Therefore, the ceria exsolution was not observed on the micrograph nor the XRD pattern of LCeNT800 shown in Figure 3 and 4b, respectively.

Generally, the main driving forces for such cation segregation, *e.g.* Sr segregation, are recognized as a combination of electrostatic interactions and elastic energy, with the latter resulting from cation size mismatch [48, 49]. Herein, to relax the elastic energy generated around the oxidized Ce^{3+} dopants that are much smaller than the host ions, cation re-arrangement would occur

spontaneously, leading to the segregation of CeO_2 on the surface. This process can be influenced by temperature, polarization, oxygen partial pressure, *etc.* [50], thus could provide means for optimization to tune the material properties. It is worth noting that the ceria segregation mechanism is in contrast to that of typical reduction induced B-site metal exsolution (from an A-site deficient perovskite), with the latter driven by the compositional difference between the surface and the bulk of the parent material.

Concerning the different exsolution behavior of CeO_2 at grain boundaries (GBs) and free surfaces (FSs), *e.g.* only GBs segregation is observed at 1300 ℃ whilst FSs exsolution becomes pronounced at lower temperatures (Figure 3), it is likely attributed to their different nucleation free energies and temperature-dependent kinetics. As GBs generally have higher free energies than FSs, they are energetically favourable locations to minimize the nucleation energy barriers [51, 52]. In some Sr-containing perovskite systems, Sr segregation has been found to initiate at the grain boundaries, followed by surface accumulation of island-like precipitates [53, 54]. Similar to Sr segregation phenomena, CeO_2 segregation from GBs at 1300 ℃ is dominating due to the lower activation energy barrier of GBs for nucleation as compared to that of FSs. As annealing temperature decreases, exsolution of ceria cubes from FSs starts to occur, most likely due to the accelerated nucleation rate at reduced temperatures (see **Figure S7**). However, the growth of ceria nuclei at either GBs or FSs will become retarded as a consequence of slowered cation diffusion kinetics at lower temperatures, which results in decreased ceria segregation level observed in Figure 4b as anmealing temperature drops.

Besides, the morphological difference in the microstructure of the exsolved ceria, *i.e.* stripes along the grain boundaries and facet-specific cubes on surfaces, is most likely determined by the local atomic geometry of the substrate. On grain surfaces, the growth of ceria is strained by the

underlying perovskite lattice, and it is thermodynamically favorable for the cerium atoms to grow epitaxially to the substrate lattice to minimise the ceria/perovskite interfacial free energy as well as the msfit strain [55, 56]. This eventually leads to the growth of cube-like ceria epitaxy. In contrast, the ceria stripes/patches exsolved at the grain boundary are less confined. Its growth appears to be more 'freely', *i.e.* not constrained to align in an 'atom-by-atom' manner to the substrate lattice, as compared to that of the surface-grown cubes.

3.3. A-site CeO_2 and B-site Ni co-exsolution

To construct the CeO_2-Ni@LCeNT heterostructure, we further reduced the CeO_2-anchored LCeNT (*e.g.* LCeNT1200) in 5% H_2/Ar at 900 ℃ for 20 hrs. **Figure 6a** displays the microstructure of the LCeNT1200 after the reduction treatment. It can be seen that a significant number of Ni NPs (~50 nm, ~25 particles per μm^2) with an even distribution have formed on the surface of the titanate perovskite. The inserted model in Figure 6a vividly illustrates the LCeNT backbone covered with uniformly exsolved CeO_2 and Ni NPs. The XRD pattern of the LCeNT1200 after the reduction is shown in **Figure S8**. One can see that reflection peaks for CeO_2 and Ni can be resolved; in the meantime, the perovskite crystalline structure of the titanate is still preserved, denoting its outstanding stability. The exsolution of Ni NPs was also observed on the LCeNT annealed at different temperatures and reduced subsequently in 5% H_2/Ar at 900 ℃ (see **Figure S9)**. These indicate that after the emergence of ceria cubes with varying extent, the titanate is still capable of forming Ni NPs on its surface upon reduction. STEM-EDS analysis was conducted at an exsolved interface to examine its element distribution with the results presented in **Figure 6(b, c).** The EDS element maps in Figure 6c confirm the presence of ceria and metallic Ni on the titanate support.

Besides the formation of Ni NPs, partial reduction of the CeO_2 cubes also occurs; from the EDS quantification analysis (Figure 6b), the atomic ratio between Ce and O in the ceria cube rises to 1: 1.54 after the reduction treatment. To examine the ceria/LCeNT interface stability against reducing atmosphere (5% H_2/Ar, 900 °C), we carried out high-resolution STEM inspections with the results shown in **Figure 6 d-f**. In Figure 6e, the lattice fringe alignment between CeO_{2-x} and the support is identical to that of the CeO_2/LCeNT interface before reduction. It seems the socketed particle-substrate interface structure is retained, indicating the good stability of exsolved ceria particles. Nevertheless, as highlighted by red arrows in Figure 6f, atomic distortions in the ceria lattice are observed. Such lattice defects are possibly due to the lattice strain accumulated during the reduction of the CeO_2 cube.

Furthermore, the Ni/LCeNT interface is inspected by STEM imaging (in **Figure 6 g-i**). As displayed in Figure 6g, the exsolved Ni NP also develops sharp and pinned interface nanostructure with the parent perovskite. In the vicinity of the Ni/LCeNT interface region, the titanate lattice appears to have a brighter contrast compared to its bulk lattice (shown in Figure 6h). This is possibly a result of the partial submergence of the Ni particle into the supporting perovskite upon exsolution, which causes lattice superimposition. Note that at the edge of the Ni/LCeNT interface in Figure 6f, a small 'neck' structure, which shares an identical atom arrangement to the host perovskite, tightly wraps up the Ni particle. The formation of the necking structure is likely due to the surface diffusion of the perovskite towards the Ni/LCeNT interface to minimize the surface energy of the system during Ni growth, similar to the particle sintering behavior reported in the literature [57]. These features pertaining to the exsolved interfaces are widely observed in many Ni exsolution-based systems and are believed to provide good anchorage for the metal particles to their host [58, 59].

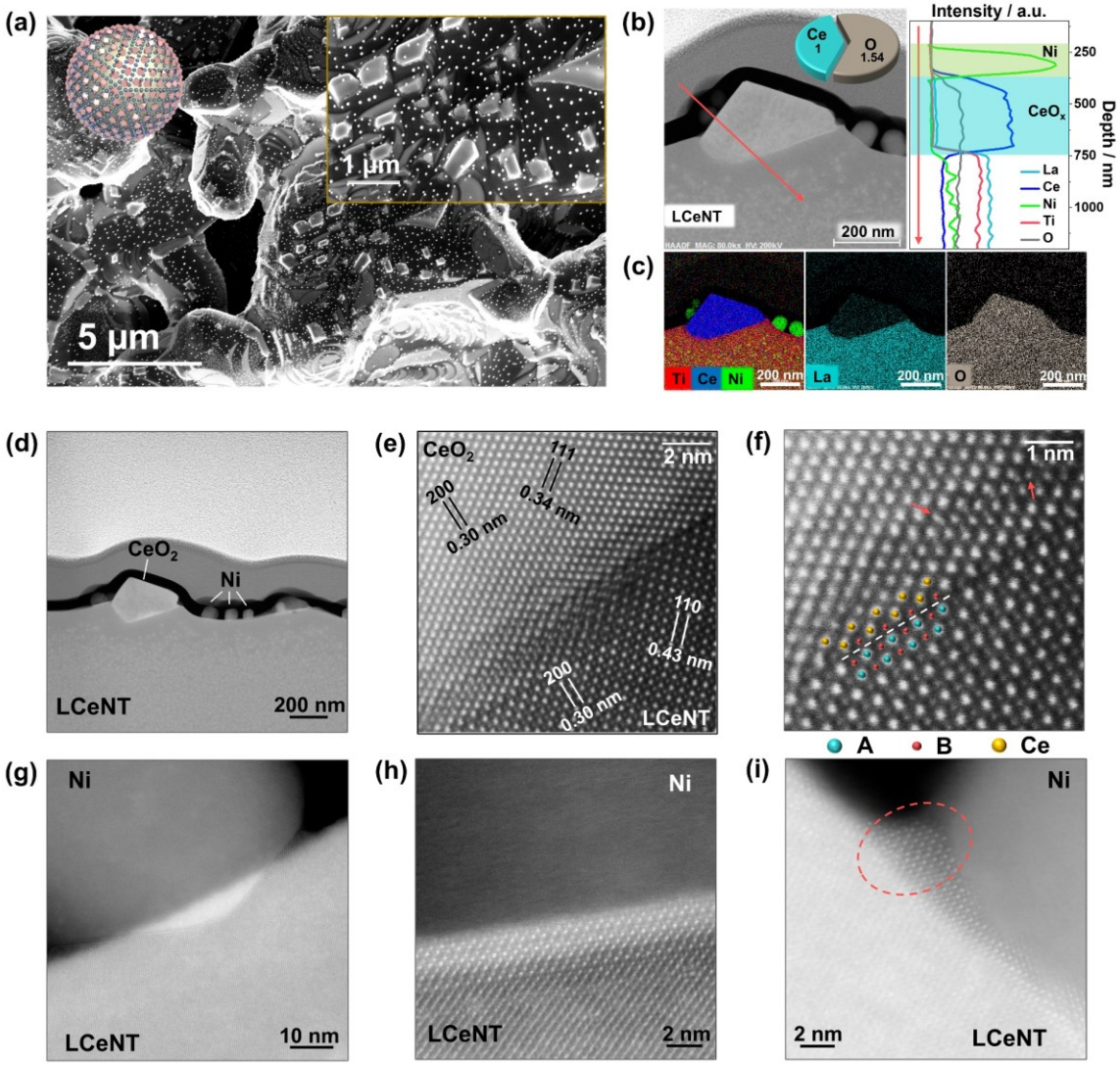

Figure 6. Microstructure and element distribution of LCeNT1200 after reduction at 900 °C for 20 hrs. (a) SEM micrographs of the titanate surfaces and the inserted model showing the exsolved titanate structure (pink: CeO_2, steel blue: Ni, gold: LCeNT); (b) STEM-HAADF image of a CeO_{2-x} cube with exsolved Ni NPs and the corresponding EDS line scan spectrum. The inserted arrows and pie chart indicate the direction of the corresponding EDS line scan and the rough atomic ratio between Ce and O, respectively; (c) STEM-EDS element mapping showing the element distribution across the exsolved titanate interface. High resolution STEM images at exsolved (d,e,f) CeO_2/LCeNT and (g,h,i) Ni/LCeNT interfaces. (e) Atomic geometry at CeO_2/LCeNT

interface and its magnified area shown in (f). The atomic arrangements of Ni/LCeNT interfaces are given in (h) central region and (i) edge region. The arrows in (f) point out two distinct atomic distortions near the interface, indicating strained ceria lattice. The dashed circle in (i) shows the neck formation at the interface edge due to perovskite surface diffusion.

3.4. Electrocatalytic performance of CeO_2-Ni@LCeNT as SOFC anode.

Following the structural characterizations, we evaluated the electrocatalytic activity of the CeO_2-Ni@LCeNT heterostructure as a potential anode material in SOFC fed with H_2 and CH_4 (3% H_2O humidified) respectively. The exsolution of both ceria and Ni is believed to be beneficial for improving the catalytic activity and stability of the titanate-based anode. It should be noted that CeO_2 cubes were introduced to the LCeNT during anode calcination (1200 °C, see Experimental for details), which was similar to the annealing treatment discussed in the previous sections. The electrochemical results, as well as the post-mortem analysis of the LCeNT single cell, are presented in **Figure 7** and **Figure 8**, respectively.

3.4.1. Catalytic activity of exsolved CeO_2 cubes

In this section, the electrochemical performance of the LCeNT cell (Cell-1) and LCNT cell (Cell-2) were evaluated. Since the LCNT electrode has no ceria but only Ni nanoparticles after reduction, the implication of CeO_2 cube growth on the cell performance can be best demonstrated by comparing these two cells. To exclude the influence of Ni exsolution, no reduction treatments were applied to either cell. In this sense, the impedance spectra of these cells were recorded at OCV at 900 °C in wet H_2 and CH_4, respectively. In **Figure 7a**, the ohmic resistances (R_Ω) of the two cells are close (0.17 *vs* 0.14 **Ω** cm^2 in H_2, 0.20 *vs* 0.16 **Ω** cm^2 in CH_4, Cell-1 and Cell-2 respectively), and the main difference is exemplified by a massive gap in the polarization

resistance (R_P). The R_P of the LCeNT cell is 3.0 and 16.3 Ω cm^2 in 3% H_2O humidified H_2 and CH_4 respectively, whereas the R_P of the LCNT cell is roughly around 39.9 Ω cm^2 in wet H_2 with a significantly larger R_P, 105.6 Ω cm^2 in wet CH_4, the value of which is more than 13 and 6 times higher than the value from the LCeNT cell in wet H_2 and methane, respectively. Apparently, the exsolved CeO_2 cubes are exceptionally instrumental in improving the electrode electrocatalytic activity in the LCeNT cell in comparison to that of the LCNT counterpart. Owing to the abundance in surface oxygen vacancy and Ce^{4+}/Ce^{3+} redox couple, ceria has been reported to possess superior activity towards the adsorption of reactant molecules and the subsequent bond activation [60]. Moreover, the CeO_2 cubes in LCeNT electrode display strong particle-substrate interactions (as discussed in previous sections), and therefore facilitated oxygen spillover effect between ceria and the support which may have played a vital role in boosting the oxygen ion exchange. Ultimately, a trivial amount of exsolved ceria (up to 3 wt.% in LCeNT) proves to be effective in catalyzing the oxidation of H_2 and CH_4 in the present study.

3.4.2. Electrochemical activity of CeO_2-Ni@LCeNT

In Cell-3, reduction treatments (*i.e.* both chemical and electrical) were employed to the LCeNT fuel electrode to construct the CeO_2-Ni@LCeNT heterostructure prior to the electrochemical evaluation. The CR treatment was carried out at 900 °C in dry 5% H_2/N_2 for 20 hrs with the resulting anode microstructure shown in **Figure S10**. The exsolution of abundant Ni NPs (46 ± 20 nm) is evidenced, in conjunction with the exsolved CeO_2 cubes on the titanate anode surface.

In addition to the CR, the fuel electrode was further reduced electrically, *i.e.* applying a 2.1 V electrolysis voltage to the cell in a 3% H_2O/H_2 atmosphere. ER treatment has been reported to reduce the titanate electrode dramatically within a few minutes due to the availability of sufficient electrons and accelerated ion diffusions. The accelerated reduction of titanate by ER results in the

exsolution of more nanocatalysts with smaller particle size and thus greatly improves electrode performance [24]. The initial R_P of the LCeNT cell before ER is 3.86 Ω cm^2 and 21.04 Ω cm^2 in humidified (~3% H_2O) H_2 and CH_4, measured under OCV conditions at 900 °C respectively (**Figure 7b**). Noting these values are slightly larger than Cell-1, and could be attributed to the deviation between cells (*e.g.* up to 10 μm difference in electrolyte thickness). Upon ER treatment, the R_P of the cell in H_2 and CH_4 drops rapidly to 0.47 Ω cm^2 and 3.75 Ω cm^2, respectively. The $R_Ω$ of the cell also experiences a slight decrease, an indication of the reduction of titanate. As a result, the peak power density (PPD) of the cell surges to 642 mW cm^{-2} in H_2 and 306 mW cm^{-2} in CH_4, increased by 150% and 53% of its initial value, respectively (see **Figure 7c**). As a comparison, a similar electrolyte-supported cell setup $La_{0.2}Sr_{0.25}Ca_{0.45}TiO_3$|ScSZ (~160 μm)|LSM-YSZ|LSM was reported by Verbraeken *et al.*, where the fuel electrode was impregnated with 10 wt% CeO_2 and 5 wt% Ni [61]. The impregnated cell showed a PPD of 290 mW cm^{-2} at 900 °C in wet H_2 (~3% H_2O), which is much less than the power output achieved from the CeO_2-Ni@LCeNT cell. Further performance comparison with similar SOFC systems is provided in **Table S1**.

Furthermore, a stability test (~20 hrs) at a constant voltage of 0.7 V for Cell-3 was done in wet CH_4 at 850 °C. This was carried out to evaluate the robustness of the CeO_2-Ni@LCeNT anode as well as its tolerance to fibrous carbon buildup. As presented in **Figure 7d**, the current density of the cell at 0.7V descends quickly initially (~1 h) before reaching an equilibrium for methane conversion. In the succeeding ~19 hrs run, a steady current density *vs* time is seen without notable degradation. An extended operation (~105 hrs) in 3% H_2O humidified CH_4 was performed on an identical cell with the results given in **Figure S11**, from which the outstanding stability of the CeO_2-Ni@LCeNT cell is also demonstrated.

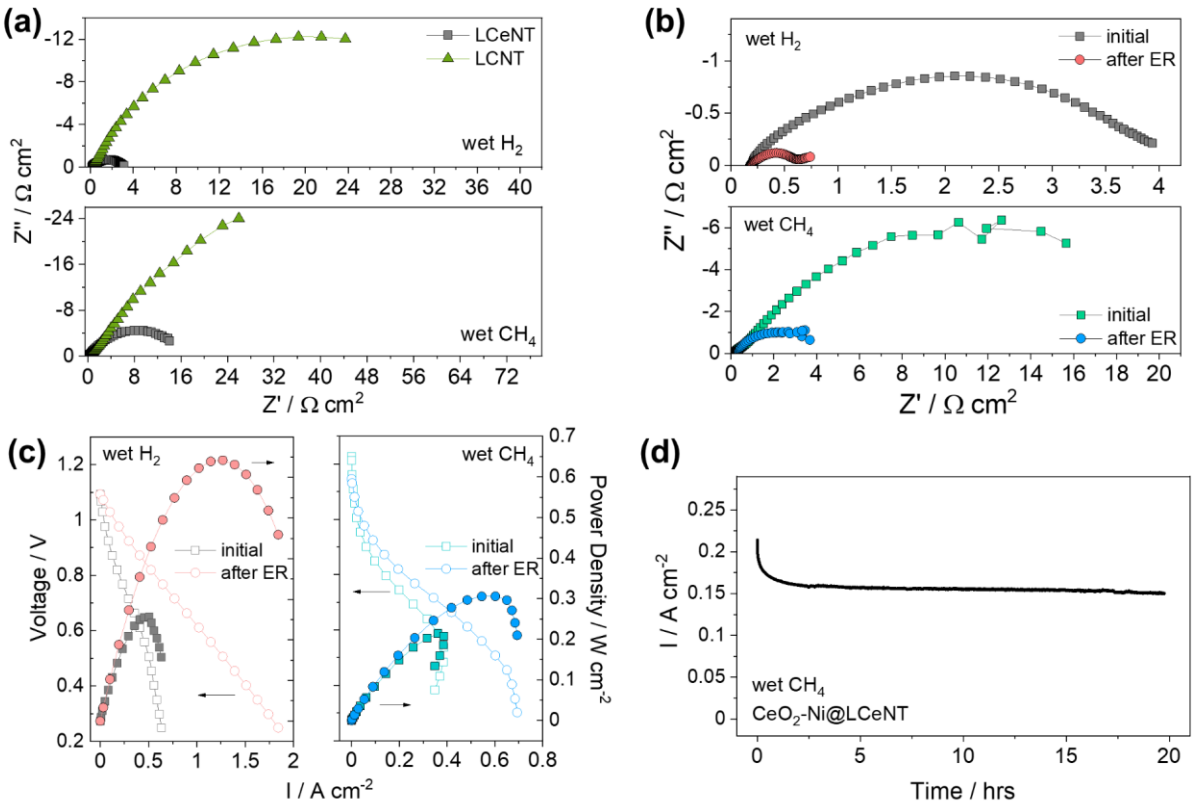

Figure 7. Electrochemical performance and stability evaluation. (a) Impedance spectra of un-reduced LCeNT (Cell-1) and LCNT (Cell-2) single cells measured in wet (3% H_2O) H_2 and CH_4 fuels at 900 °C; (b) Impedance spectra and (c) I-V curves of the CR-treated LCeNT single cell (Cell-3) at 900 °C, before and after ER treatment; (d) Short-term stability of Cell-3 measured in wet CH_4 fuel at 0.7 V at 850 °C.

3.4.3. Post-mortem analysis

Figure 8a presents the XRD pattern of the LCeNT fuel electrode from Cell-3 after testing. Reflection peaks that pertain to the ScSZ electrolyte and Au current collector are resolved. The perovskite structure persists in the LCeNT fuel electrode after the chemical/electrochemical reduction and the stability test, reflecting its exceptional stability in solid oxide cell application. Noting that CeO_2, Ni and NiO peaks are also observable in Figure 8a. The appearance of NiO

reflections suggests partial oxidation of the Ni NPs while cooling down the cell from high temperature. The presence of partially oxidized Ni NPs is evidenced by the corresponding STEM-EDS element mapping results as well (see **Figure S12**).

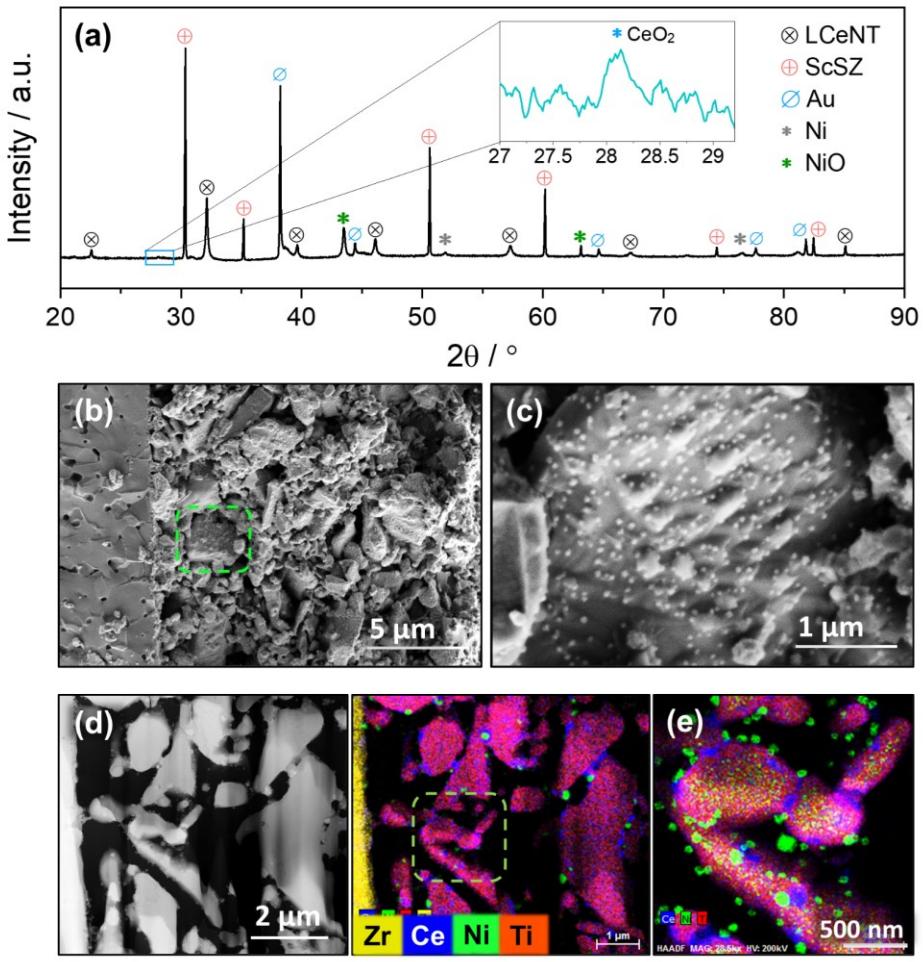

Figure 8. Post-mortem structure analysis. (a) Room temperature XRD pattern of the CeO_2-Ni@LCeNT anode of the tested Cell-3 specimen; (b) SEM micrograph of the cross-section of the cell at anode/electrolyte side, and (c) a magnified region of the anode in (b); (d) Cross-sectional STEM-EDS analysis of the cell at the anode/electrolyte side, and (e) a zoom-in area of the anode.

With respect to the microstructure, **Figure 8 b** and **c** reveal the post-mortem SEM micrograph of the anode and the topography of a typical anode particle, respectively. Well-pinned CeO_2 and

Ni (or NiO) NPs of considerable amount can be seen on the anode support, similar to those found on pellet samples (Figure 6a). Noting that the particle size of Ni NPs (48 ± 23 nm) stays close to the pre-test state (46 ± 20 nm). This indicates once again the remarkable thermal stability of *in situ* grown NPs. Moreover, a cross-sectional STEM-EDS analysis was performed at the anode/electrolyte side, where the elemental distribution is characterized (see **Figure 8d**). A zoomed-in EDS map of the anode confirms the uniform decoration of the titanate by a large amount of CeO_2 and Ni NPs (**Figure 8e**). It is worth mentioning that based on the SEM and STEM examination, no fibrous carbon is discernible on the anode, which corroborates our early conjecture that the CeO_2-Ni@LCeNT heterostructure has superior coking resistance. As explained before, both exsolved CeO_2 and Ni NPs exhibit a well-pinned and coherent interface structure with the LCeNT substrate (see Figure 2f and 7h). Such strong particle-substrate interactions were found responsible for the exceptional anti-coking properties of a similar exsolved Ni/$La_{0.52}Sr_{0.28}Ni_{0.06}Ti_{0.94}O_3$ heterointerface, observed after being exposed in dry 20% CH_4/H_2 atmosphere for 4 hrs at 800 ℃ [29].

3.4.4. Implications of CeO_2 and Ni exsolution on fuel electro-oxidation

Intuitively it is postulated that the exsolved CeO_2 and Ni NPs function in tandem toward the catalytic adsorption and activation of H_2 or CH_4 molecules, see **Figure 9** where a schematic mechanism for H_2/CH_4 oxidation on LCeNT is shown. Since they both individually show good catalytic activity toward fuel oxidation, a synergistic effect may be in place for catalyzing the reactant molecules. Focusing on methane oxidation in SOFCs, it is accepted that multiple competing processes, *e.g.* partial oxidation, oxidative coupling, cracking, internal reforming and direct oxidation would occur concurrently in the anode chamber [62, 63]. Although determining each reaction pathway has been challenging due to the complexity of the system, a sequence of

elementary steps can be proposed to describe methane oxidative dehydrogenation. It is generally acknowledged that methane oxidation includes steps of hydrogen extraction toward the formation of chemisorbed carbon and hydrogen species on the catalyst surface [64], as illustrated in **Figure 9**, and subsequent oxidation of the absorbed species by O^{2-} flux through the electrolyte in SOFCs, as shown below:

$$CH_{4(g)} + (5-x)^* \rightarrow CH_x^* + (4-x)H^*,\ x = 0 \sim 4 \quad (5)$$

$$C^* + O^* \rightarrow CO^* + * \quad (6)$$

$$CO^* + O^* \rightarrow CO_{2(g)} + 2^* \quad (7)$$

$$2H^* + O^* \rightarrow H_2O_{(g)} + 3^* \quad (8)$$

where * denotes the active site on the catalyst surface. Equation 8 also applies to H_2 fuel oxidation. A thermodynamic calculation has predicted that methane partial/complete oxidation is dominant under SOFC operation conditions especially with dry feed [65], thus internal reforming is not discussed here for simplification. According to previous studies, the rate-limiting step of methane oxidation is the initial breakage of the first C-H bond to form an adsorbed methyl group (Equation 5, x = 3) [66]. Regarding LCeNT electrode, the exsolution of CeO_2 cubes has improved performance, significantly outweighing the ceria-absent LCNT counterpart (Cell-1 vs. Cell-2, see Figure 7a). The abundant active sites and lattice oxygen supplied by ceria nanocubes may have facilitated the CH_4 absorption and oxidation processes on the anode surface. Nevertheless, reports suggested that ceria alone cannot provide sufficiently high catalytic activity for methane activation in practical applications [67, 68], thus the addition of an effective catalyst, such as Ni which possesses intrinsic ability to break C-H bonds is essential [69]. Indeed, further exsolution of Ni NPs on LCeNT anode (Cell-3) has induced markedly enhanced performance towards both H_2 and CH_4 electro-oxidation, demonstrating nearly one order of magnitude lower R_P than that of the anode without Ni NPs (Cell-1, see Figure 7 a-c). It is worth noting that Ni alone favors carbon

deposition due to its ability to catalyze C-C bond formation and the considerable solubility of carbon, while CeO_2 is known as an effective catalyst to suppress/remove carbon deposits *via* Equation 6 and 7 [70, 71]. The combination of CeO_2 and Ni NPs appears to be advantageous in preventing fibrous carbon buildup (see Figure 8).

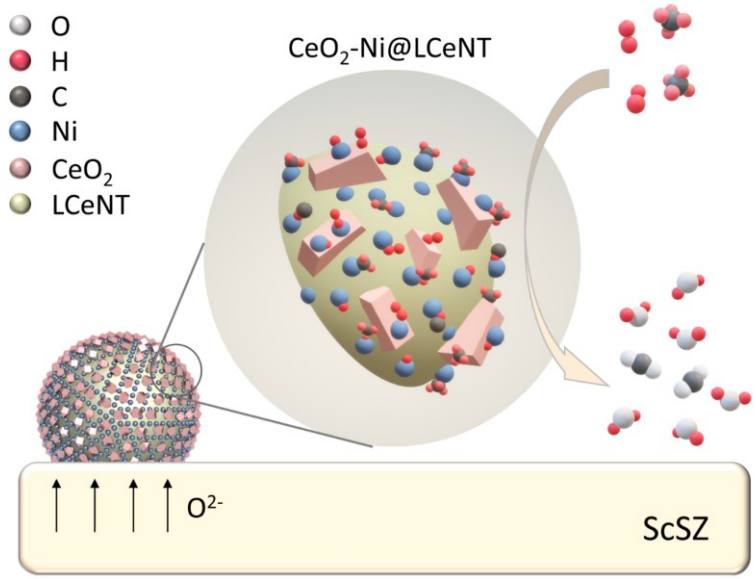

Figure 9. The possible catalytic tandem effect from CeO_2 and Ni NPs for boosting H_2 and CH_4 electrochemical conversion.

Moreover, both CeO_2 and Ni NPs exhibit strained structure with the titanate support, *i.e.* strong catalyst-support interactions (Figure 2 and Figure 6), which have been widely recognized to greatly affect the reaction pathways as well as the product distribution during methane (and hydrogen) catalysis [72, 73]. It is explained by oxygen adatom transfer from the support to the NPs surface or *vice versa*, a process known as the spillover effect [74]. In addition to the ion exchange, catalyst-support interactions also involve electron donation or back-donation between the NPs and the surface adsorbate. As electron transfer alters the chemisorptive bond strength of the surface species, such electronic effects were suggested to play an equally important part in facilitating

methane (and hydrogen) catalysis [66]. As a consequence, the heterostructured titanate displays satisfactory electrochemical performance as SOFC anode and yet, there is great room for improvement, *e.g.* by optimizing the LCeNT particle size and the resulting electrode microstructure as well as by varying ER conditions, which will be reported in future.

4. Conclusion

In this work, we demonstrated a viable approach to constructing the CeO_2-Ni@titanate heterostructure *in situ* with stable and controllable nanoscale architectures. We firstly highlighted that abundant growth of faceted CeO_2 cubes (*e.g.* ~50 nm in size, ~20 particles per μm^2 in coverage) from the titanate could be realized via a simple air-annealing treatment (*e.g.* electrode calcination in SOFCs), with the exsolution of densely packed Ni NPs (~50 nm, ~25 particles per μm^2) taking place following a subsequent reduction in 5% H_2/Ar.

We further revealed that the morphology of exsolved ceria cubes, *i.e.* size and population, depends greatly on annealing temperature. When annealed in the range of 1300 - 900 ℃, lower temperature led to the growth of finer but more CeO_2 cubes, *e.g.* ~220 nm, ~1 particles per μm^2 at 1200 ℃ *vs* ~130 nm, ~9 particles per μm^2 at 1100 ℃. Moreover, the exsolved CeO_2 cubes displayed pronounced faceting, featuring $\{111\}_{CeO2}$ and $\{200\}_{CeO2}$ terminating planes. A coherent interface structure was established between the ceria epitaxy and the titanate substrate, reflecting an inherently strong particle-substrate interaction. It was speculated that the successful incorporation of Ce in LCeNT perovskite during synthesis was most likely ascribed to a thermal reduction process (*i.e.* $Ce^{4+} \rightarrow Ce^{3+}$), and the subsequent air-annealing led to the oxidation of Ce^{3+}. The undersized Ce^{4+} cations were then segregated due to the perovskite lattice strain relaxation.

Finally, the CeO_2-Ni@LCeNT heterostructure was evaluated as a potential fuel electrode in H_2- and/or CH_4-fed SOFCs. Compared to an electrode without exsolved ceria, the LCeNT electrode displayed significantly higher performance for H_2/CH_4 oxidation, due to the superior catalytic activity from the strained ceria nanocubes formed on the surface of the LCeNT support. The electrolyte-supported cell utilizing CeO_2-Ni@LCeNT as fuel electrode yielded a satisfactory maximum power density of 642 mW cm^{-2} and 306 mW cm^{-2} at 900 °C in humidified H_2 and CH_4 fuels (~3% H_2O) respectively, attributed to enhanced electrocatalytic properties from both the exsolved ceria and Ni nanoparticles. Superior structural and chemical robustness of the material was substantiated by a short-term (~20 hrs) stability test in methane and subsequent post-mortem analysis. It thus demonstrated the promising application of the CeO_2-Ni@LCeNT nanohybrid as, but not limited to fuel electrode material in SOFCs.

In a word, we believe that the surface re-structuring strategy exemplified here sets a facile example to construct active ceria-metal/titanate heterostructure and provides insights for the future design of more sophisticated oxide systems.

CRediT authorship contribution statement

Shuai He: Conceptualization, Methodology, Writing - original draft. **Meng Li**: Visualization, Investigation, Writing - review & editing. **Jianing Hui**: Investigation, Writing - review & editing. **Xiangling Yue**: Conceptualization, Supervision, Funding acquisition, Writing - review & editing.

Declaration of Competing Interest

The authors declare no competing financial interest.

Acknowledgments

The authors would like to thank the EPSRC UKRI Innovation Fellowship EP/S001891/1 for funding, and the EPSRC Capital for Great Technologies Grant EP/L017008/1 for financial support.

Appendix A. Supplementary data

TEM image of a typical FIB lamella in Figure S1; BSE image of the cross-section of the fabricated fuel cell in Figure S2; STEM-EDS analysis of the as-prepared LCeNT in Figure S3; SEM-EDS analysis of the rLCeNT in Figure S4; XRD Rietveld refinement of LCeNT annealed at different temperatures in Figure S5; BSE images of LCeNT1300 and LCeNT1200-1400 in Figure S6; temperature denpendence of nucleation rate graph in Figure S7; XRD pattern of reduced LCeNT1200 in Figure S8; SEM images of the co-exsolved LCeNT surfaces in Figure S9; Microstructure of the CR-treated LCeNT cell in Figure S10; Extended operation of durability test of CeO_2-Ni@LCeNT cell with CH_4 fuel in Figure S11; STEM-EDS mapping of CeO_2-Ni@LCeNT anode in Cell-3 in Figure S12; a comparison of cell performance data in Table S1.

References

[1] P. Kanhere, Z. Chen, Molecules 19 (2014) 19995-20022.
[2] S. Stramare, V. Thangadurai, W. Weppner, Chem. Mater. 15 (2003) 3974-3990.
[3] K.B. Yoo, G.M. Choi, Solid State Ionics 180 (2009) 867-871.
[4] J. Sunarso, S.S. Hashim, N. Zhu, W. Zhou, Prog. Energy Combust. Sci. 61 (2017) 57-77.
[5] D.S. Deak, Mater. Sci. Technol. 23 (2013) 127-136.
[6] J.J. Alvarado Flores, M.L. Ávalos Rodríguez, G. Andrade Espinosa, J.V. Alcaraz Vera, Int. J. Hydrogen Energy 44 (2019) 12529-12542.
[7] S.P. Jiang, S.H. Chan, J. Mater. Sci. 39 (2004) 4405-4439.
[8] S. Hui, A. Petric, J. Electrochem. Soc. 149 (2002) J1-J10.
[9] A. Atkinson, S. Barnett, R.J. Gorte, J.T.S. Irvine, A.J. McEvoy, M. Mogensen, S.C. Singhal, J. Vohs, Nat. Mater. 3 (2004) 17-27.
[10] A. Rothschild, W. Menesklou, H.L. Tuller, E. Ivers-Tiffée, Chem. Mater. 18 (2006) 3651-3659.
[11] D. Neagu, J.T.S. Irvine, Chem. Mater. 22 (2010) 5042-5053.
[12] O. Marina, Solid State Ionics 149 (2002) 21-28.
[13] D. Neagu, J.T.S. Irvine, Chem. Mater. 23 (2011) 1607-1617.

[14] Z. Liu, D. Ding, B. Liu, W. Guo, W. Wang, C. Xia, J. Power Sources 196 (2011) 8561-8567.
[15] H. Kurokawa, T.Z. Sholklapper, C.P. Jacobson, L.C. De Jonghe, S.J. Visco, Electrochem. Solid-State Lett. 10 (2007).
[16] L. Lu, C. Ni, M. Cassidy, J.T.S. Irvine, J. Mater. Chem. A 4 (2016) 11708-11718.
[17] D. Neagu, G. Tsekouras, D.N. Miller, H. Menard, J.T.S. Irvine, Nat. Chem. 5 (2013) 916-923.
[18] J.T.S. Irvine, D. Neagu, M.C. Verbraeken, C. Chatzichristodoulou, C. Graves, M.B. Mogensen, Nat. Energy 1 (2016) 15014.
[19] Y. Sun, J. Li, Y. Zeng, B.S. Amirkhiz, M. Wang, Y. Behnamian, J. Luo, J. Mater. Chem. A 3 (2015) 11048-11056.
[20] O. Kwon, S. Sengodan, K. Kim, G. Kim, H.Y. Jeong, J. Shin, Y.W. Ju, J.W. Han, G. Kim, Nat. Commun. 8 (2017) 15967.
[21] T. Zhu, H.E. Troiani, L.V. Mogni, M. Han, S.A. Barnett, Joule 2 (2018) 478-496.
[22] B.H. Toby, R.B. Von Dreele, J. Appl. Crystallogr. 46 (2013) 544-549.
[23] G. Tsekouras, D. Neagu, J.T.S. Irvine, Energy Environ. Sci. 6 (2013) 256-266.
[24] J.H. Myung, D. Neagu, D.N. Miller, J.T.S. Irvine, Nature 537 (2016) 528-531.
[25] M. Chanthanumataporn, J. Hui, X. Yue, K. Kakinuma, J.T.S. Irvine, K. Hanamura, Electrochim. Acta 306 (2019) 159-166.
[26] M. WoŁcyrz, L. Kepinski, J. Solid State Chem. 99 (1992) 409-413.
[27] M. Kovacevic, B.L. Mojet, J.G. van Ommen, L. Lefferts, Catal. Lett. 146 (2016) 770-777.
[28] T. Akita, M. Okumura, K. Tanaka, M. Kohyama, M. Haruta, J. Mater. Sci. 40 (2005) 3101-3106.
[29] D. Neagu, T.S. Oh, D.N. Miller, H. Menard, S.M. Bukhari, S.R. Gamble, R.J. Gorte, J.M. Vohs, J.T.S. Irvine, Nat. Commun. 6 (2015) 8120.
[30] D. Neagu, E.I. Papaioannou, W.K.W. Ramli, D.N. Miller, B.J. Murdoch, H. Menard, A. Umar, A.J. Barlow, P.J. Cumpson, J.T.S. Irvine, I.S. Metcalfe, Nat. Commun. 8 (2017) 1855.
[31] D.J. Cumming, V.V. Kharton, A.A. Yaremchenko, A.V. Kovalevsky, J.A. Kilner, J. Am. Ceram. Soc. 94 (2011) 2993-3000.
[32] G. Subodh, J. James, M.T. Sebastian, R. Paniago, A. Dias, R.L. Moreira, Chem. Mater. 19 (2007) 4077-4082.
[33] X.-W. Zhou, Y.-F. Sun, G.-Y. Wang, T. Gao, K.T. Chuang, J.-L. Luo, M. Chen, V.I. Birss, Electrochem. Commun. 43 (2014) 79-82.
[34] Y.-F. Sun, X.-W. Zhou, Y. Zeng, B.S. Amirkhiz, M.-N. Wang, L.-Z. Zhang, B. Hua, J. Li, J.-H. Li, J.-L. Luo, J. Mater. Chem. A 3 (2015) 22830-22838.
[35] C. Périllat-Merceroz, G. Gauthier, P. Roussel, M. Huvé, P. Gélin, R.-N. Vannier, Chem. Mater. 23 (2011) 1539-1550.
[36] H. Xu, Y. Wang, J. Nucl. Mater. 265 (1999) 117-123.
[37] L.A.J. Garvie, P.R. Buseck, J. Phys. Chem. Solids 60 (1999) 1943-1947.
[38] M. Colella, G.R. Lumpkin, E.R. Vance, G.W. Hong, C.J. Kim, J. Mater. Sci. Lett. 21 (2002) 1797-1801.
[39] R.C. Karnatak, J. Esteva, H. Dexpert, M. Gasgnier, P.E. Caro, L. Albert, Phys Rev B Condens Matter 36 (1987) 1745-1749.
[40] D.J. Cumming, Cerium-doped strontium titanate materials for solid oxide fuel cells, Department of Materials, Imperial College London, 2009.
[41] T. Kodama, N. Gokon, Chem. Rev. 107 (2007) 4048-4077.
[42] M. Sturzenegger, P. Nüesch, Energy 24 (1999) 959-970.
[43] M. Lundberg, Int. J. Hydrogen Energy 18 (1993) 369-376.
[44] S. Lorentzou, G. Karagiannakis, D. Dimitrakis, C. Pagkoura, A. Zygogianni, A.G. Konstandopoulos, Energy Procedia 69 (2015) 1800-1809.
[45] N. Gokon, S. Sagawa, T. Kodama, Int. J. Hydrogen Energy 38 (2013) 14402-14414.
[46] B. Bulfin, A.J. Lowe, K.A. Keogh, B.E. Murphy, O. Lübben, S.A. Krasnikov, I.V. Shvets, J. Phys. Chem. C 117 (2013) 24129-24137.
[47] M. Peng, Z. Pei, G. Hong, Q. Su, Chem. Phys. Lett. 371 (2003) 1-6.

[48] W. Lee, J.W. Han, Y. Chen, Z. Cai, B. Yildiz, J. Am. Chem. Soc. 135 (2013) 7909-7925.
[49] B. Koo, K. Kim, J.K. Kim, H. Kwon, J.W. Han, W. Jung, Joule 2 (2018) 1476-1499.
[50] J. Friedel, Adv. Phys. 3 (1954) 446-507.
[51] Y.R. Jo, B. Koo, M.J. Seo, J.K. Kim, S. Lee, K. Kim, J.W. Han, W. Jung, B.J. Kim, J. Am. Chem. Soc. 141 (2019) 6690-6697.
[52] D.A. Porter, K.E. Easterling, Phase transformations in metals and alloys, Chapman & Hall, London; New York, 1992.
[53] H. Tellez, J. Druce, T. Ishihara, J.A. Kilner, ECS Trans. 72 (2016) 57-69.
[54] M. Niania, R. Podor, S.J. Skinner, J.A. Kilner, ECS Trans. 68 (2015) 665-670.
[55] O.I. Lebedev, G.V. Tendeloo, S. Amelinckx, H.L. Ju, K.M. Krishnan, Philos. Mag. A 80 (2000) 673-691.
[56] K.J. Kim, H. Han, T. Defferriere, D. Yoon, S. Na, S.J. Kim, A.M. Dayaghi, J. Son, T.S. Oh, H.M. Jang, G.M. Choi, J. Am. Chem. Soc. 141 (2019) 7509-7517.
[57] M. Cologna, R. Raj, J. Am. Ceram. Soc. 94 (2011) 391-395.
[58] D. Neagu, V. Kyriakou, I.L. Roiban, M. Aouine, C. Tang, A. Caravaca, K. Kousi, I. Schreur-Piet, I.S. Metcalfe, P. Vernoux, M.C.M. van de Sanden, M.N. Tsampas, ACS Nano 13 (2019) 12996-13005.
[59] S. He, K. Chen, M. Saunders, J. Li, C.Q. Cui, S.P. Jiang, J. Electrochem. Soc. 164 (2017) F1437-F1447.
[60] B. Li, S. He, J. Li, X. Yue, J.T.S. Irvine, D. Xie, J. Ni, C. Ni, ACS Catalysis 10 (2020) 14398-14409.
[61] M.C. Verbraeken, B. Iwanschitz, A. Mai, J.T.S. Irvine, J. Electrochem. Soc. 159 (2012) F757-F762.
[62] Y. Takagi, K. Kerman, C. Ko, S. Ramanathan, J. Power Sources 243 (2013) 1-9.
[63] B. Tu, X. Su, Y. Yin, F. Zhang, X. Lv, M. Cheng, Fuel 278 (2020).
[64] J. Wei, E. Iglesia, J. Phys. Chem. B 108 (2004) 7253-7262.
[65] J.-H. Koh, B.-S. Kang, H.C. Lim, Y.-S. Yoo, Electrochem. Solid-State Lett. 4 (2001).
[66] T.M. Gür, Prog. Energy Combust. Sci. 54 (2016) 1-64.
[67] S. Souentie, M. Athanasiou, D.K. Niakolas, A. Katsaounis, S.G. Neophytides, C.G. Vayenas, J. Catal. 306 (2013) 116-128.
[68] J.-H. Myung, H.-J. Ko, J.-J. Lee, J.-H. Lee, S.-H. Hyun, Int. J. Hydrogen Energy 37 (2012) 11351-11359.
[69] T.-J. Huang, M.-C. Huang, Chem. Eng. J. 135 (2008) 216-223.
[70] O.A. Marina, M. Mogensen, Appl. Catal., A 189 (1999) 117-126.
[71] T.-J. Huang, C.-H. Wang, J. Power Sources 163 (2006) 309-315.
[72] J.B. Miller, M. Malatpure, Appl. Catal., A 495 (2015) 54-62.
[73] F.B. Passos, E.R. Oliveira, L.V. Mattos, F.B. Noronha, Catal. Lett. 110 (2006) 161-167.
[74] W.C. Conner, J.L. Falconer, Chem. Rev. 95 (2002) 759-788.